ACSNANO

www.acsnano.org

ARTICLE

Phosphorus-Rich Copper Phosphide Nanowires for Field-Effect Transistors and Lithium-Ion Batteries

Guo-An Li,[†] Chiu-Yen Wang,[‡] Wei-Chung Chang,[†] and Hsing-Yu Tuan*[,†]

[†]Department of Chemical Engineering, National Tsing Hua University, Hsinchu, Taiwan 300

[‡]Department of Materials Science and Engineering, National Taiwan University of Science and Technology, Taipei 106, Taiwan

Supporting Information

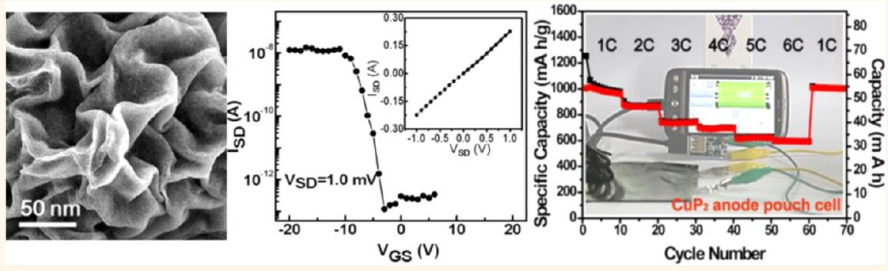

ABSTRACT: **Phosphorus-rich transition metal phosphide CuP_2 nanowires were synthesized with high quality and high yield (~60%) via the supercritical fluid−liquid−solid (SFLS) growth at 410 °C and 10.2 MPa. The obtained CuP_2 nanowires have a high aspect ratio and exhibit a single crystal structure of monoclinic CuP_2 without any impurity phase. CuP_2 nanowires have progressive improvement for semiconductors and energy storages compared with bulk CuP_2. Being utilized for back-gate field effect transistor (FET) measurement, CuP_2 nanowires possess a p-type behavior intrinsically with an on/off ratio larger than 10^4 and its single nanowire electrical transport property exhibits a hole mobility of 147 $cm^2 V^{-1} s^{-1}$, representing the example of a CuP_2 transistor. In addition, CuP_2 nanowires can serve as an appealing anode material for a lithium-ion battery electrode. The discharge capacity remained at 945 mA h g^{-1} after 100 cycles, showing a good capacity retention of 88% based on the first discharge capacity. Even at a high rate of 6 C, the electrode still exhibited an outstanding result with a capacity of ~600 mA h g^{-1}. *Ex-situ* transmission electron microscopy and CV tests demonstrate that the stability of capacity retention and remarkable rate capability of the CuP_2 nanowires electrode are attributed to the role of the metal phosphide conversion-type lithium storage mechanism. Finally, CuP_2 nanowire anodes and $LiFePO_4$ cathodes were assembled into pouch-type lithium batteries offering a capacity over 60 mA h. The full cell shows high capacity and stable capacity retention and can be used as an energy supply to operate electronic devices such as mobile phones and mini 4WD cars.**

KEYWORDS: *metal phosphide, copper diphosphide, semiconductor nanowires, transistor, lithium-ion battery*

Metal phosphides (MP_x) have emerged as a technically important class of materials for their wide range of applications and promising properties such as magnetism,[1,2] optics,[3−7] and energy storage.[8−14] They can form various binary phases with compositions from metal-rich to phosphorus-rich (~M_6P to MP_4) as phosphorus atoms are able to exist as single anions or larger polyphosphide anions due to direct P−P bonding.[15−17] Structures with a variety of forms associated with the M/P ratio are typically semiconductor and diamagnetic. Different stoichiometrics of metal phosphides result in diverse properties. For instance, metal-rich phosphides such as Fe_2P are typically metallic, while polyphosphides such as FeP_2 are often small bandgap semiconductors.[18]

Compared to their bulk sizes, nanomaterials have shown incredible properties, different geometries, and enhanced performance on the fields of catalysis, electronic devices, and energy storages.[19−23] For example, one-dimensional nanostructures show improved performance as lithium ion battery anodes due to shorter lithium ion diffusion length and higher contact area with the electrolyte. 1-D nanostructures effectively tolerate relaxed mechanical strain along with alleviating pulverization and provide a fast electron conducting pathway. As a building block for transistor device, nanowires play the role of a bridge

Received: June 15, 2016
Accepted: September 7, 2016
Published: September 7, 2016

DOI: 10.1021/acsnano.6b03954
ACS Nano 2016, 10, 8632−8644

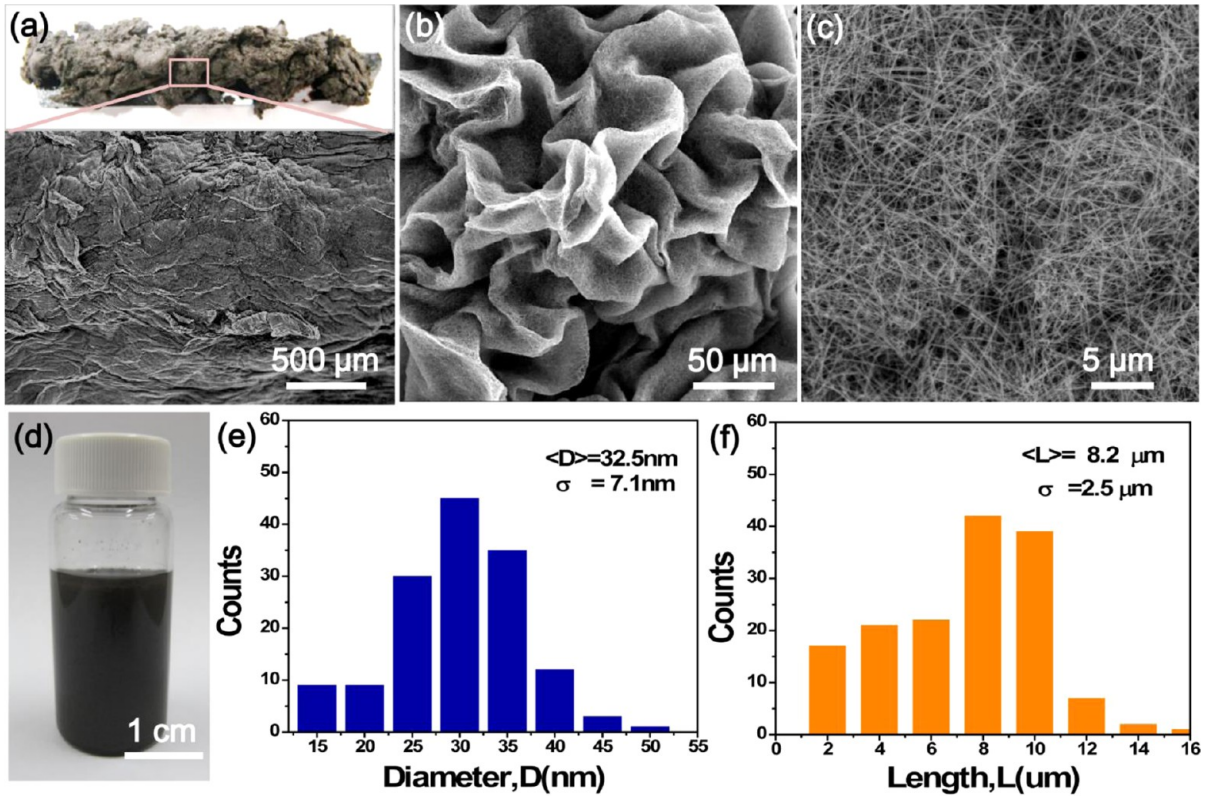

Figure 1. SFLS-grown CuP_2 nanowires produced with copper chloride, TOP, and Bi precusor in benzene at 410 °C and 10.2 MPa. (a–c) Different magnified SEM images to observe the surface morphology of the CuP_2 nanowires product. Inset of Figure 1a shows a photograph of CuP_2 nanowires on silicon substrate. (d) After cleaning with ethanol, CuP_2 nanowires can be well dispersed in toluene. (e) Statistics of CuP_2 nanowire diameter. (f) Statistics of CuP_2 nanowire diameter length.

connecting to larger scale metallization and effectively improving device parameters such as the carrier mobility and transconductance.[24−27]

Among numerous metal phosphides, the binary copper phosphide (CuP_2) is a promising material in the field of lithium ion batteries and semiconductor transistors. Metal phosphide can react with lithium through a mechanism called conversion reaction, which involve the redox of metallic nanoparticles and matrix Li_3P as follows:

$$MP_x + 3xLi \rightarrow M^0 + xLi_3P$$

From the conversion reaction equation, each P atom in metal phosphide can react with three lithium ions to form one Li_3P compound with a high specific capacity of 2596 mA h g^{-1}, suggesting phosphorus-rich compounds more suitable for lithium ion batteries than metal-rich ones based on energy density concerns.[28−31] Simultaneously, the higher lithiation potential prevents batteries from lithium plating during fast charging. CuP_2 possesses high specific volumetric capacity due to its material density (ρ = 4.31 g/cm^3). In the demand of high energy density and power density in lithium ion batteries, CuP_2 is a remarkable alternative anode material for commercial graphite. In the field of field effect transistors (FETs), it has reported that CuP_2 exists as a p-type semiconductor with a hall mobility of 60 cm^2 V^{-1} s^{-1} at room temperature and possesses a diamagnetism nature,[32,33] which are related to the structure feature of the compound; however, a transistor device has yet to be made until now.

However, very few studies have reported on the synthesis and application of CuP_2.[34] CuP_2 could be synthesized by a chemical vapor phase transport method in which copper and red phosphorus with stoichiometric amounts react in a sealed ampule with Cl_2, by a flux method growth using metal as solvent, or by a direct high energy ball-milling technique.[32] These strategies were carried out at high temperature and harsh reaction conditions or it was difficult to separate CuP_2 from impurity products. In addition, the quality of CuP_2 synthesized in the literature reports is still not suitable for technological applications. For example, CuP_2 showed extremely poor electrochemical performance while it reacted with lithium entirely in the first charging step, exhibiting a capacity of 1325 mA h g^{-1} and severely fading to 400 mA h g^{-1} after 15 cycles.[35] The unstable cycle retention was due to the pulverization of bulk CuP_2 induced by huge volume variance with lithium intercalation/deintercalation during charge/discharge cycling. Besides, there have been few studies to explore the relationship between structure and property and related applications in nanotechnology.[36]

Here, we report the synthesis of CuP_2 nanowires *via* a supercritical fluid−liquid−solid growth (SFLS) by using an organic mixture of copper chloride (CuCl) and tri-*n*-octylphosphine (TOP) as precursor, and bismuth precursor as the metal seed source. High yield in the proximity of 60% of CuP_2 nanowires was obtained in one batch experiment. As-prepared CuP_2 nanowires have a length of several micrometers and diameter of tens of nanometers. Meanwhile, CuP_2 nanowires are air-stable and exhibit a monoclinic structure without any other impurity phase. In addition, CuP_2 nanowires' dual applications for FET devices and lithium ion batteires are demonstrated. A single CuP_2 nanowire transistor exhibits p-

DOI: 10.1021/acsnano.6b03954
ACS Nano 2016, 10, 8632−8644

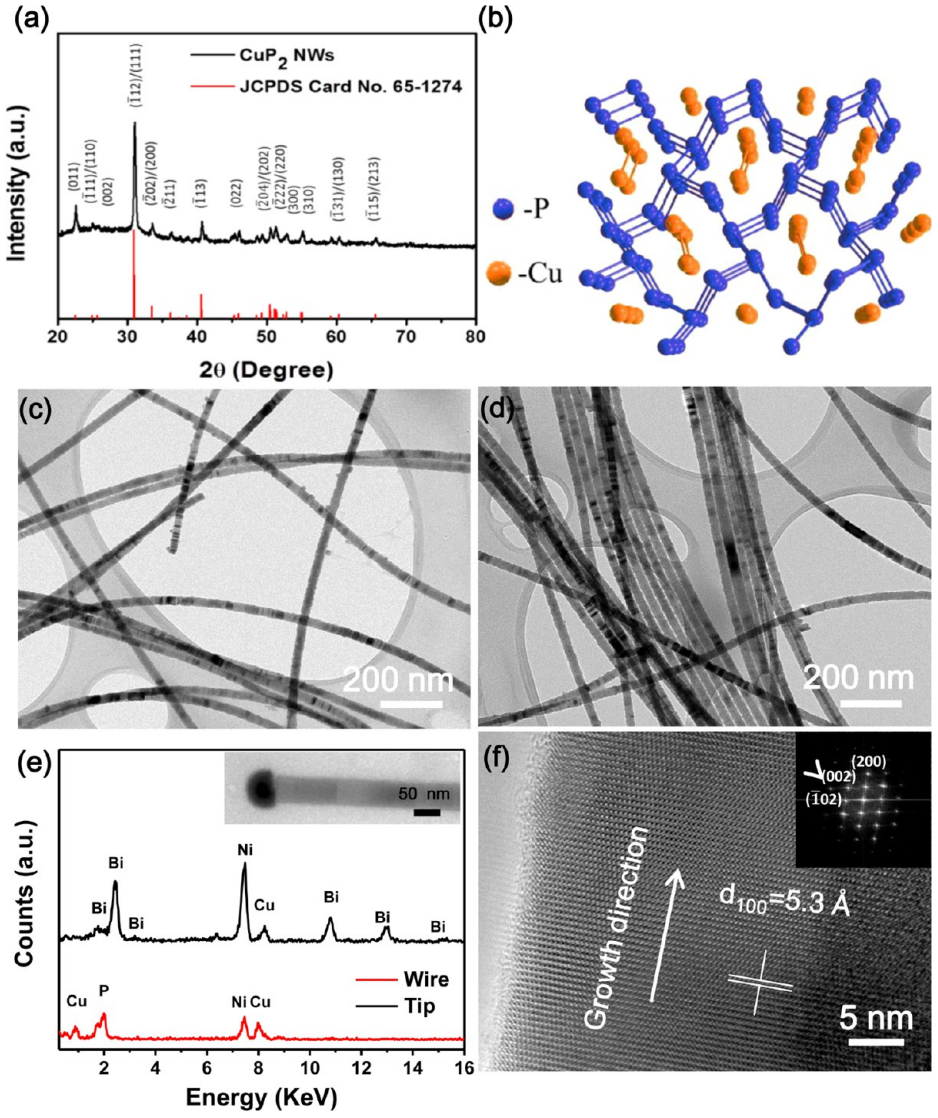

Figure 2. (a) XRD pattern and (b) structural representation of monoclinic CuP_2 nanowire. (c,d) TEM, (e) EDS, and (f) HRTEM images of CuP_2 nanowires. Inset shows the FFT pattern.

type behavior and an on/off ratio larger than 10^4. The field-effect hole mobility of CuP_2 nanowires is 147 $cm^2\ V^{-1}\ s^{-1}$ higher than that of the bulk counterpart (60 $cm^2\ V^{-1}\ s^{-1}$). CuP_2 nanowires as an anode material in the lithium ion batteries showed a reversible capacity of nearly 1000 mA h g^{-1} at 0.1 C rate (1 C = 1 Ag^{-1}), corresponding to 2.7 times higher than the theoretical capacity of graphite (372 mA h g^{-1}). Even at high rate of 6 C, the performance was still outstanding with a capacity of 600 mA h g^{-1}. Finally, CuP_2 anode material and $LiFePO_4$ cathode material were assembled into a full cell and the battery performance was examined comprehensively, which gives conceptual demonstration for the feasibility of CuP_2 nanowire for commercial applications.

RESULTS AND DISCUSSIONS

CuP_2 Nanowires Characterization. CuP_2 nanowires were synthesized in supercritical benzene at 410 °C and 10.2 MPa (102 atm) by reacting copper chloride and tri-*n*-octylphosphine in the presence of a bismuth precursor. Approximately 65 mg of product throughput with a high yield of 60% was collected on a silicon substrate in one semibatch reaction, which is shown in Figure 1a. Observed from SEM images (Figure 1a–c), CuP_2 nanowires entangle into an irregular wave-like surface without any perceptible amount of particulate byproducts. The product was brown and can be well dispersed in toluene without precipitation after brief sonication (Figure 1d). Regarding the morphology of CuP_2 nanowires, the diameter of the wires, 32.5 ± 2.3 nm, was obtained by statistical analysis over 200 CuP_2 nanowires measured from SEM images. The length of tangled wires was generally up to tens of micrometers with aspect ratios greater than 200 (Figure 1e,f).

The XRD pattern of CuP_2 nanowire powder has structures similar to that of AgP_2 with the same space group of $P21/c$ as shown in Figure 2a.[37] The crystalline monoclinic structure of CuP_2 (lattice constants: a = 5.802 Å, b = 4.807 Å, c = 7.525 Å, and β = 112.68°; JCPDS 65-1274) was readily recognized from all the diffraction peaks. Moreover, no other phases, such as Cu_3P or Cu_2P_7, were detected. Figure 2b shows the simulated structural demonstration of monoclinic CuP_2. In the structure, the copper atoms were shown as covalently bonded Cu–Cu dumbbells and were located in the octahedral holes in the

DOI: 10.1021/acsnano.6b03954
ACS Nano 2016, 10, 8632–8644

middle of the layers made of puckered, 2-D sheets of fused P_{10}^{5-} rings.

The detailed morphology and the structure of CuP_2 nanowires were further evidenced by TEM and HRTEM. Tortuous nanowires were spread without any impurity (Figure 2c). Nevertheless, some nanowires with neat orientation in small self-assemblies along their axial direction were found, which were shown in Figure 2d. Most probably, steric repulsive interaction between adjacent nanowires is weakened, which is induced by partial removal of surface-capping ligand TOPs during the synthetic process, and CuP_2 nanowires are subject to self-assembly.[38] The inset of Figure 2e is a TEM image of a stick of nanowire with a dark particle at the tip. Element characterization was confirmed by energy-dispersive X-ray spectroscopy (EDS) of the nanowire shown in Figure 2e (EDS mapping shown in Figure S1). The signals of Cu, P, and Bi element detected correspond to the wire and tip, respectively, thus implying the nanowire growth through the SFLS mechanism.

The obtained products are crystalline characterized by high-resolution transmission electron microscopy (HRTEM) and X-ray diffraction (XRD). The HRTEM image (Figure 2f) reveals that the spacing of lattice fringes perpendicular to the preferential growth direction ⟨100⟩ was 0.53 nm matching with the lattice spacing of (100) planes in bulk CuP_2. The fast Fourier transform (FFT) pattern of the nanowire also was indexed to the monoclinic structure in inset of Figure 2f, with a zone axis of [010]. In the TEM observation, there are about 10% nanowires with stacking fault found in the product, similar to those observed in GaP and GaAs nanowires.[39,40] Alternating light/dark contrasts appear along the nanowire growth direction (Figure 3a) and HRTEM images (Figure 3b,c) show the alternating crystal structure with repetition of twin planes along the nanowires. From Figure 3d, the defects are confined to a single complete (100) plane and ⟨02⟩ and ⟨20$\bar{2}$⟩ directions symmetrically reflect from the ⟨100⟩ direction at the twin boundary. Figure 3e,f depicted the FFTs of TEM images above and below the twin boundary. The twinning faults are attributed to some reaction parameters such as precursor concentration or the temperature fluctuated during nanowire growth.

Various reaction temperatures were used to explore the optimal growth conditions and growth mechanism of CuP_2 nanowires. The synthesis of CuP_2 nanowires at temperatures varying from 350 to 550 °C under a pressure of 10.2 MPa was compared. The synthesis carried out at 350 °C did not yield wires on silicon substrate (Figure 4a). The outcome product was the solution with the slightly brown color as a previous precursor, implying a Cu−TOP complex was intact, and decomposed rarely at this temperature. At different reaction temperatures ranging from 400 to 450 °C, the product mostly consisted of high quality wires (Figure 4b−d), representing the optimum temperature region for nanowire growth reaction. In reactions with temperatures exceeding 500 °C (Figure 4e,f), there existed wires hundreds of nanometers in diameter with poor crystallininty and some amorphous microspheres. As far as we know, the particulate products were attributed to severe homogeneous nucleation reactions. This suggested that nanowire growth is maintained but that homogeneous nucleation of the microspheres becomes a competing mechanism and severely affects the quality of the nanowires. At the higher temperature, no wires were found. The synthesis possessed sufficient energy to carry out homogeneous particulate

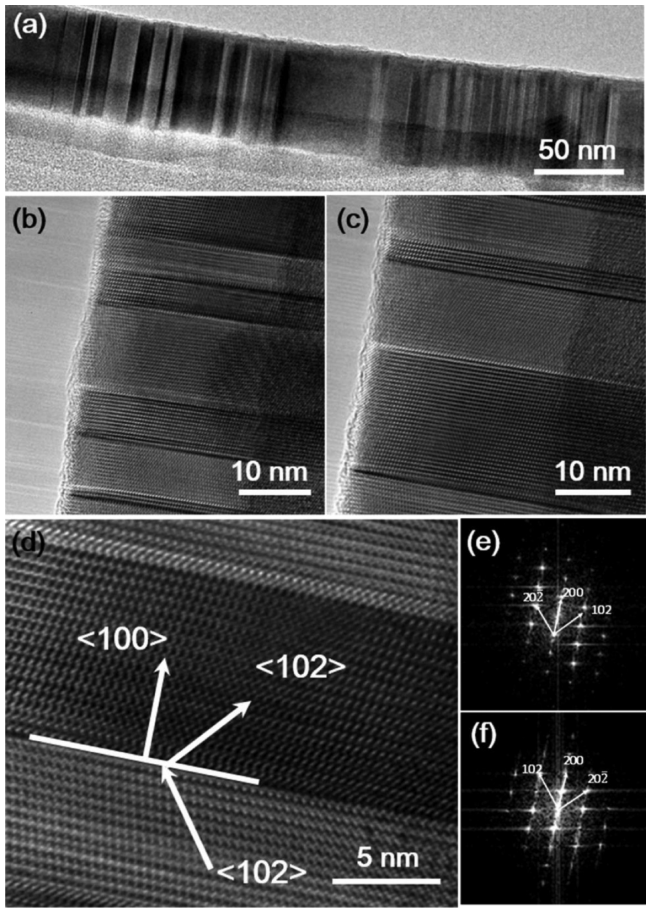

Figure 3. (a) TEM, (b,c) HRTEM images of CuP_2 nanowire with stacking faults perpendicular to the axial direction. (d) HRTEM images of a fault plane with FFTs of the image (e) above and (f) below the fault plane.

formation instead of heterogeneous nanowire growth. Reactions with other precursors, including copper bromide, copper iodine, and copper acetylacetonate, were also carried out to make a comparison for the formation of CuP_2 nanowires (Supporting Information, Figure S2). From the observation of TEM images, nanowires obtained from copper bromide and iodide result in large distributions. On the other hand, nanowires obtained from copper acetylacetonate result in poor crystallinity. These results showed these precursors are not suitable for CuP2 nanowires.[41,42]

X-ray photoelectron spectroscopy (XPS) analysis was also used to investigate the surface states of CuP_2 nanowires and the chemical environment. Known from the XPS data (Supporting Information, Figure S3), the CuP_2 nanowires are stable and free of oxide signals, even at exposure to atmosphere at least for one month. Because CuP_2 is one kind of polyphosphide compound comprising a 10-membered phosphorus ring with a sharing edge, Zintl−Klemm rules were applied to count electrons to dtermine the bonding, in which CuP_2 shows a Cu^{1+} oxidation state and $P^{0.5-}$ reduction state.[43] In these experiments, the binding energy of the copper and phosphorus 2p 3/2 electrons was investigated. The copper binding energy was 933.1 eV, definitely in the region of metal state Cu^0 (932.2−932.7 eV) and oxidized state Cu^{2+} (936.0−937), showing a reduction in metal ($Cu^{<1+}$), associated with partially covalent bonding between the copper and phosphorus atoms. The experimental

DOI: 10.1021/acsnano.6b03954
ACS Nano 2016, 10, 8632−8644

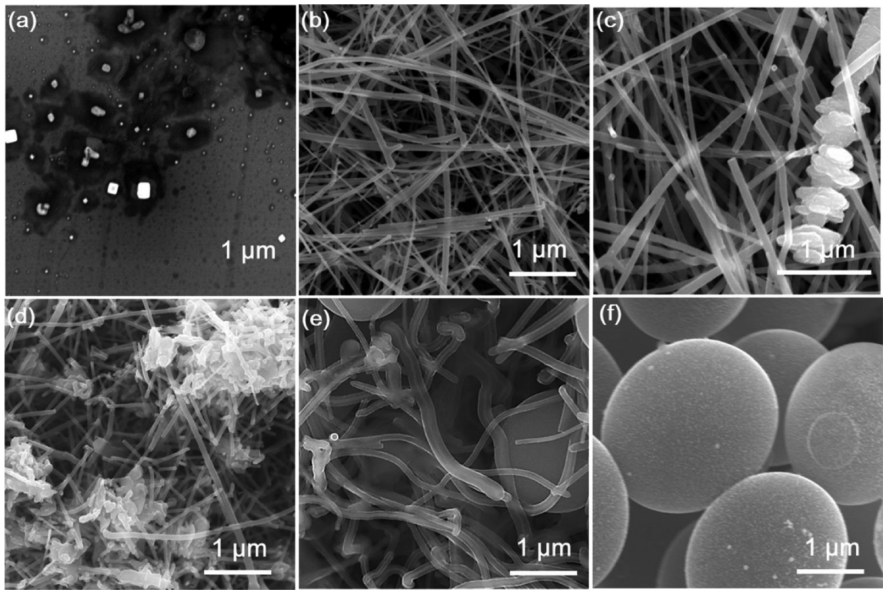

Figure 4. SEM images of CuP_2 nanowires synthesized in benzene at 10.2 MPa (102 atm) under various reaction temperature (a) 350, (b) 400, (c) 430, (d) 450, (e) 500, and (f) 550 °C.

P 2p 3/2 binding energy was 129.8 eV, indicating an oxidation state resembling elemental state P.

A back-gate FET was manufactured to examine the electrical transport property of CuP_2 nanowires as illustrated in Figure 5a. Electronic properties of CuP_2 nanowires at ambient temperature were obtained through a current−voltage plot for V_g = 0 V as shown in Figure 5b. The curve of 80 nm-sized nanowire exhibited a linear dependence, estimating a resistance of 1.58×10^6 Ω. Then we utilize the formula $R = \rho LA^{-1}$ to calculate the resistivity (7.9×10^{-3} Ω m), where R, A, and L correspond to the resistivity of the material, the nanowire cross-sectional area, and length, respectively. Compared with the intrinsic resistivity of bulk CuP_2 (10^{-3} Ω m) at room temperature, CuP_2 nanowires show the relatively larger resistivity. Figure 5c shows a logarithm plot of the $I_{SD}-V_{GS}$ curve. From the plot, CuP_2 nanowire FET behavior is p-type with a high on/off ratio of 10^4. The relationship between the drain current I_{SD} and drain voltage V_{DS} in Figure 5b was perfectly linear which suggests ohmic contact between Ni and CuP_2 nanowires.[44] Using a cylinder on an infinite plate model,[45] we estimate the capacitance between the CuP_2 and the back-gate oxide to be

$$C_{ox} = \frac{2\pi\varepsilon_{ox}\varepsilon_0 L}{\cosh^{-1}\left(\frac{r + t_{ox}}{r}\right)}$$

where $\varepsilon_{ox} = 8.85 \times 10^{-14}$ F cm^{-1} is the vacuum dielectric constant, $\varepsilon_0 = 3.9$ is the relative dielectric constant for SiO_2, L (1 μm) and r (40 nm) correspond to effective length and radius of the CuP_2 nanowire, respectively, and the thickness of back-gate dielectric (t_{ox}) is 330 nm. The gate capacitance is $C_{ox} = 7.44 \times 10^{-17}$ F. From the $I_{SD}-V_{GS}$ curve, the field effect hole mobility was obtained employing the transconductance (g_m) at a fixed drain bias V_{SD}:[46−48]

$$\mu = \frac{g_m L^2}{V_{SD} C_{ox}}$$

At drain bias V_{DS} = 1 mV, the maximum transconductance gained from the Figure 5c is 1.1 nS, exhibiting a hole mobility of 147 cm^2 V^{-1} s^{-1}.

The electrochemical properties of the as-synthesized CuP_2 nanowires were investigated by assembling them into a coin-type half-cell. Figure 6a shows that cycling performance of CuP_2 nanowires versus Li metal tested at a current density of 0.1 C rate (0.1 A g^{-1}; C/n denotes n hours to finish a half cycle) in the voltage window of 0.02−2.5 V at ambient temperature. The first charge and discharge capacity were 1530 and 865 mA h g^{-1}, respectively, which indicates a coulombic efficiency of 57%. The irreversible capacity loss in the first cycle was probably attributed to the consumption of lithium in the formation of the solid electrolyte interface (SEI) layer.[49,50] On charging to reduction potentials of organic carbonates in the electrolyte, the SEI layer was formed on the anode surface. The passivating layer is a lithium-ion condutor but insulating to electrons. During the subsequent cycle, the capacity retention of as-prepared CuP_2 nanowires drops rapidly. We speculated that the poor result is caused by active material detached from current collector due to the aggregation of nanomaterials during charge/discharge.[51,52] As a result, as-prepared CuP_2 nanowires were executed in a calcination process at 450 °C under N_2 with no phase change evidenced by the XRD analysis (Supporting Information, Figure S4). The CuP_2 nanowires' capping ligand TOP decomposed into the carbon shell on the active surface, and it has been reported that the amorphorous carbon shell from the calcination step significantly improves electrochemical and suppresses the aggregation of active materials.[53] With the aid of a protective layer, the mechanical strength of the CuP_2 nanowires was enhanced at the same time and effectively tolerates the volume expansion with an improvement of capacity retention and reduced electrode resistivity.[54−56] Indeed, great progress in electrochemical performance was made for CuP_2 nanowires (Supporting Information, Figure S6). The first charge and discharge capacity were 1689 and 1075 mA h g^{-1} respectively, with a coulombic efficiency of 64%. With subsequent cycles, coulombic efficiency remains at a high level of ∼98%,

DOI: 10.1021/acsnano.6b03954
ACS Nano 2016, 10, 8632−8644

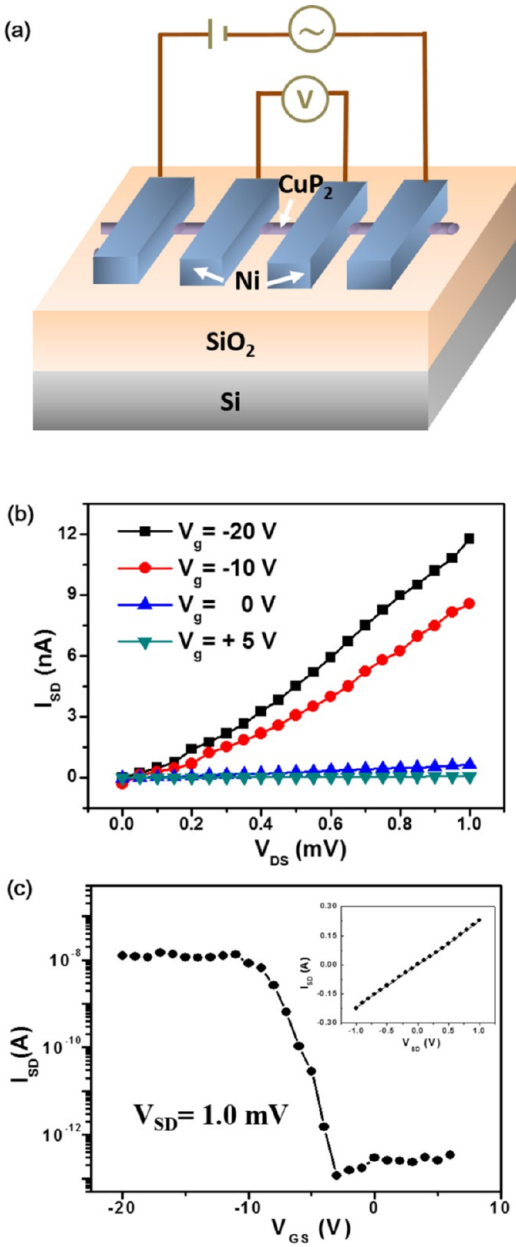

Figure 5. As-fabricated CuP_2 nanowire FET at room temperature: (a) schematic illustration of as-deposited CuP_2 nanowires device structure; (b) I_{SD}−V_{DS} curves of the back-gate CuP_2 nanowire transistor; (c) I_{SD}−V_{GS} curves of back-gate transistor.

demonstrating a great reversibility between the charge and discharge. The capacity for the 100th cycle was 945 mA h g^{-1}, with an average capacity decay of 0.12% per cycle, showing good capacity retention. On the basis of the superior result after thermal treament, we regard the calcinated CuP_2 nanowire as anode material for lithium ion batteries in the following electrochemical experiment, unless otherwise specified in the context.

In the meantime, the voltage versus capacity profiles of CuP_2 nanowires for the first three cycles were obtained at Figure 6b. For the first cycle charging, two peaks located at 0.6 and 0.72 V corresponding to the phase transformation of CuP_2 due to lithium-ion insertion were found. In the subsequent cycle, the voltage plateau is shifted to 0.75 V, associated with conversion reaction,[57,58] followed by a gently decreasing slope until 0.02 V. Apparently, the voltage profiles are consistent with each other for the following cycles showing high reversibility. As for the discharging process, all voltage curves show similar locus with two small reaction plateaus located at 1.12 and 1.25 V related to the removal of the lithium-ion from active materials.

Rate capability is another essential parameter for many practical applications of lithium ion batteries such as electric vehicles and tools. In general, high rate tests showed that higher polarization and subsequent capacity fade dramatically for cell resistance.[59,60] In our study, CuP_2 nanowires exhibit excellent electrochemical performance even at high current. Figure 6c shows the rate cycling behavior of CuP_2 nanowires at various current density including 0.2, 0.5, 1, 2, 4, and 6 C, respectively, and repeats the loop setting four times. As charge/discharge current density increased, the capacity of the cell decreased indistinctly. Even with the cell cycled at a 6 C rate, the capacity maintained approaching 600 mA h g^{-1}, which is still larger than the theoretical capacity of graphite for commercial anodes. When the C-rate returned to 0.2 C, the capacities of CuP_2 showed about 1000 mA h g^{-1} with a capacity retention of 87%, indicating extraordinarily high cycling stability. At the same time, we executed electrochemical tests for the CuP_2 electrode with 0.2 C for charging to pair up different discharge current densities including 0.2, 0.5, 1, 2, 4, 6, 8, and 10 C (Figure 6d). The results showed excellent high rate performance with a capacity of 850 mA h g^{-1} at 10 C. In addition, long cycle life at a high rate is an indicative test for lithium-ion batteries. Figure S8 represents the cycling performance of CuP_2 nanowires electrode with a current density of 1 C. Initially, charging and discharging capacity correspond to 1359 and 1017 mA h g^{-1}, respectively. The capacity reversibility of electrode maintains well during cycling and discharge capacity still shows 800 mA h g^{-1}. There seemed to a capacity loss (~20%) after 200 cycles of charging and discharging processes. The coin type cell was disassembled to look through the situation of an anode electrode. Apparently, the material of the electrode was detached from the current collector and some cracks appeared in the electrode shown in Figure S9. Probably, the fast capacity fade is induced by repetitive volume variances during charging and discharging. Repetitive behavior of lithium insertion and removal caused the active material electrical disconnection and delamination physically. To tackle this issue, the recipe for an anode electrode slurry was slightly tuned (CuP_2/super-p/binder is 65:15:20 in wt %) to carry out the cycling life curve at 4 C for 500 cycles (Figure 6e). Initially, the current density 0.1 C for the first cycle was employed to form a fine SEI layer on the anode surface. At the 500th cycle, the retention of CuP_2 nanowires' specific capacity maintained 81.3% based on the fifth cycle (specific capacity: 703 mA h g^{-1}), showing an improvement of stability for the cycling life curve with the aid of appropriate amount of binder. From the above-mentioned, CuP_2 nanowires showed outstanding high rate test results in lifespan and reversibility, which imply CuP_2 nanowires indeed maintain structure stability without exfoliation from the current collector and possess fast electron transfer due to treatment with calcination of CuP_2 nanowires.

Electrochemical impedance spectroscopy (EIS) was executed to investigate interfacial electrochemical behavior of CuP_2-based electrodes during the cycling test with different charge/discharge cycles for 0.1C rate at frequencies from 10 kHz to 10 mHz. The Nyquist plots, composed of semicircles at the high frequency region and a straight line slope at low frequency regions, were interpreted by a proper electric equivalent circuit

DOI: 10.1021/acsnano.6b03954
ACS Nano 2016, 10, 8632−8644

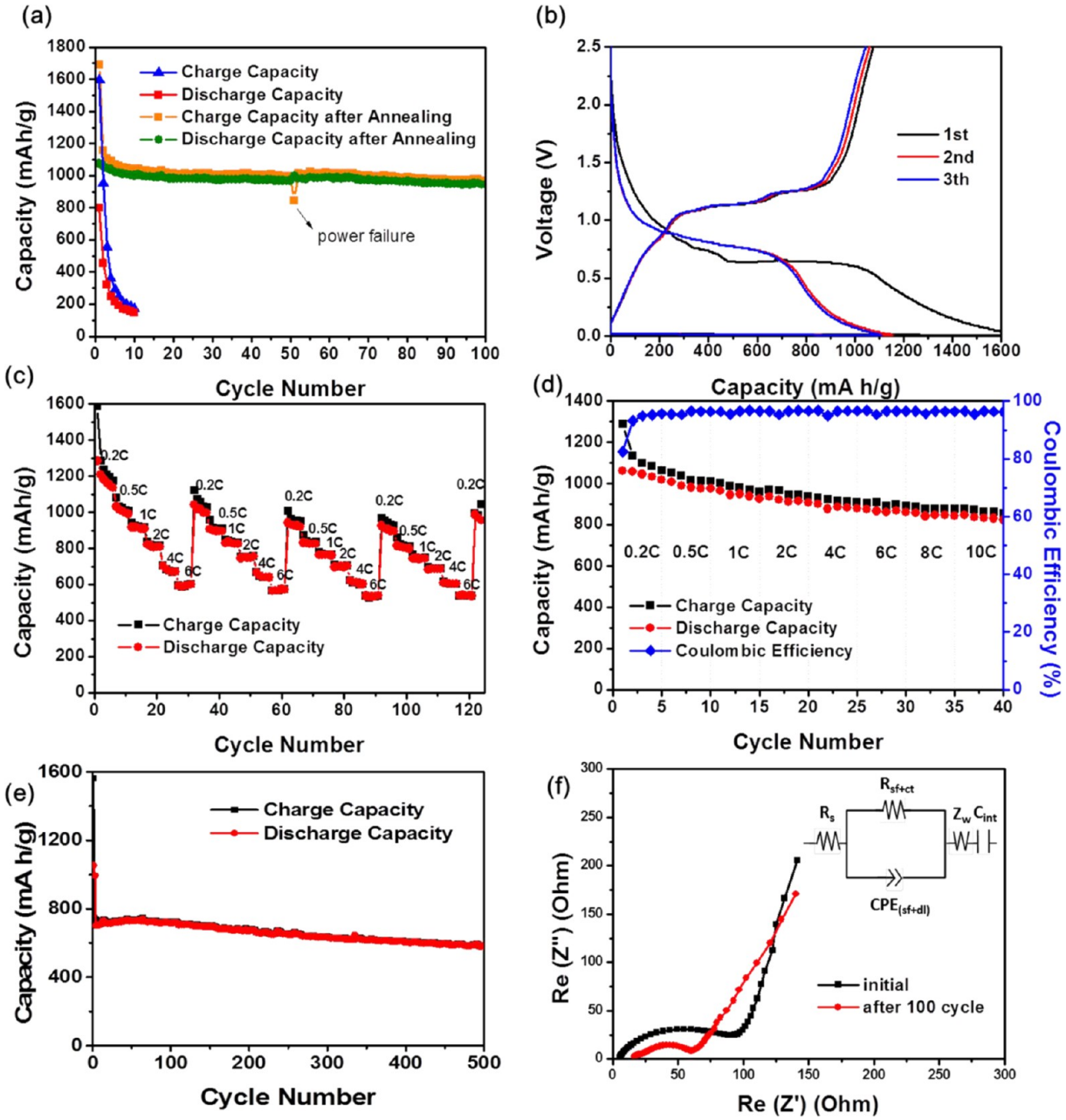

Figure 6. (a) Charge/discharge cycle performance of calcinated CuP_2 nanowires and no calcinated CuP_2 nanowires, at a rate of 0.1 C between 0.01 and 2.5 V. (b) Galvanostatic charge/discharge profiles of calcinated CuP_2 nanowire at 0.1 C rate for the first three cycles. (c) Rate capability test including 0.2, 0.5, 1, 2, 4, and 6 C with multiple cycle execution. (d) Charge/discharge cycle performance at the same charge current density (0.2 C) and various discharge cureent density of of 0.2, 0.5, 1, 2, 4, 6, 8, and 10 C. Charge/discharge cycle performance of calcinated CuP_2 nanowires at a rate of 1 C for 200 cycles. (e) Binder was increased slightly for the anode electrode to test the cycling life curve at a current density of 4 C (0.1 C for the first cycle) for 500 cycles with a retention of 81.3% based on the 5th cycle (specific capacity at 5th and 500th is 703 and 570 mA h g^{-1}, respectively) between 0.01 and 2.5 V. (f) Electrochemical impedance spectroscopy of calcinated CuP_2 nanowire electrode with fresh and after 50 cycles charge/discharge cycling test.

shown in the inset of Figure 6f. Interception with the real impedance axes corresponded to 5.6 and 16.6 Ω, respectively, in the Nyquist plots (Figure 6f) of CuP_2 electrodes at different cycles (fresh electrode, after 100 cycles). This resistance represents ohmic resistance related to conductivity of electrolyte and geometry of electrode.[61] As frequency decreases, there is a semicircle called charge transfer resistance, indicating that the electrode is polarized when its potential is apart from its equilibrium value at the open circuit. The electrode showed the smaller diameter of the semicircle after 100 cycles, which suggests that the fresh electrodes possess the larger charge transfer resistance. Charge transfer resistance decreased from 95 to 50 Ω after 100 cycles, indicating electrode structure transformation favorable to electron transfer and lithium ion diffusion in the electrode during cycling.[62] The sloping region that follows represents Warburg impedance, which is diffusion resistance of the electrolyte ions into the electrode. The slope increased at the low frequency region after 100 cycles, implying a decreased diffusion resistance due to generation of facile lithium diffusion channels, probably associated with the

DOI: 10.1021/acsnano.6b03954
ACS Nano 2016, 10, 8632–8644

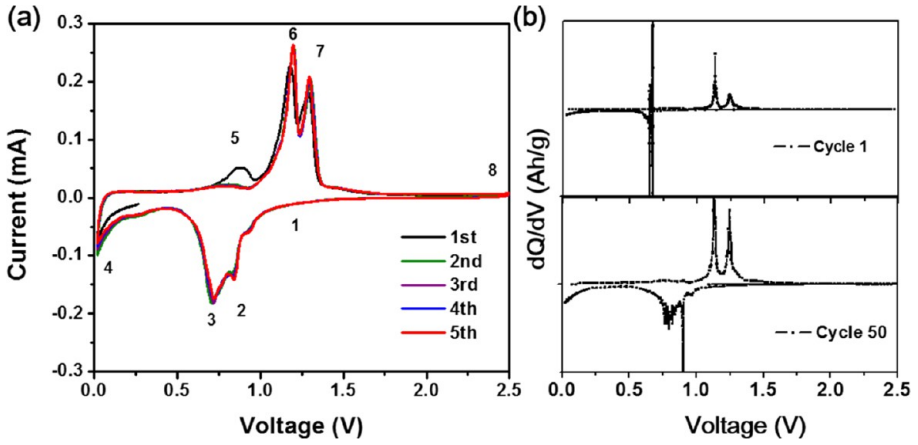

Figure 7. (a) The cyclic voltammograms of CuP_2 nanowires in the first 5 cycles with a scan rate of 0.5 mV s^{-1} at room temperature. (b) The differential capacity versus voltage of the 1st cycle and 50th cycle derived from the galvanostatic curves of CuP_2 nanowires at 0.1 C rate at room temperature.

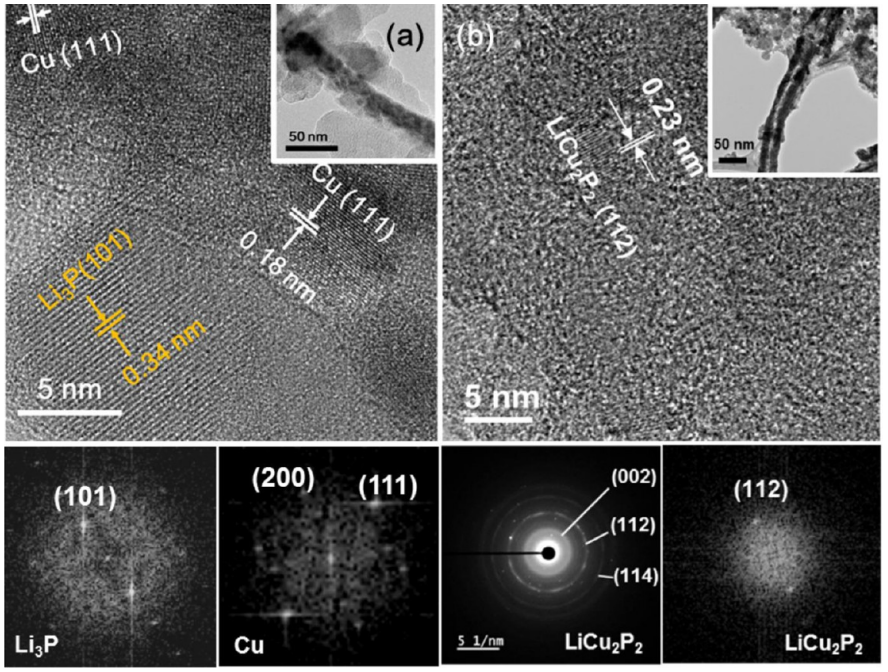

Figure 8. *Ex-situ* TEM analysis of the CuP_2 nanowire electrode reaction with lithium (a) fully charging to 0.02 V. FFT pattern of Li_3P and Cu. (b) Fully discharging to 2.5 V. FFT and SAED pattern of $LiCu_2P_2$.

formation of the Li ion conductive matrix Li_3P during charge/discharge.[63]

All the above results well reveal that the CuP_2 nanowire is a superior anode material for extremely high power and energy lithium ion batteries.

CuP_2 reacts with lithium through a conversion reaction to form the transition metal nanoparticles and matrix-like Li−P compound. The briefly mechanism can be described as follows:

$$CuP_2 + 6Li^+ + 6e^- \rightarrow Cu + 2Li_3P \quad (1)$$

Figure 7a demonstrates the cyclic voltammetry of CuP_2 nanowires electrode in the top five cycles. It is obvious from this figure that the redox peaks resemble the peaks in the differential capacity vs voltage plot Figure 7b,c. Initially, when the voltage declined from open circuit voltage, two small peaks around 0.8 V showed up, which represent the insertion reaction. We speculated that the Li ion reacted with CuP_2 to form $LiCu_2P_2$ and LiP phases. Then the potential around 0.7 V was believed to be due to the Cu and different Li_xP phases, such as LiP, LiP_7, LiP_5, and Li_3P_7, associated with the conversion reaction.[28,64] When the CuP_2 nanowires electrode was fully charged to 0.02 V, the final phase Cu and Li_3P appeared. Further, the electrode reversely discharged to 2.5 V, there exists a small peak at 0.9 V probably related to irreversibility because of some SEI formation. The peaks located at 1.23 and 1.27 V are attributed to the lithium-ion removal from the Li_3P to form $LiCu_2P_2$ phase.

In the meantime, *ex-situ* TEM analysis was conducted to provide assistant evidence for the reaction mechanism and further understand the structure transformation of CuP_2 with lithium. The interplanar spacings calculated from Figure 8a are indexed to Cu (0.18 nm) and Li_3P (0.34 nm), respectively, which are in good agreement with the lattices from JCPDS database as shown in Table S3. Observed from the TEM image,

DOI: 10.1021/acsnano.6b03954
ACS Nano 2016, 10, 8632−8644

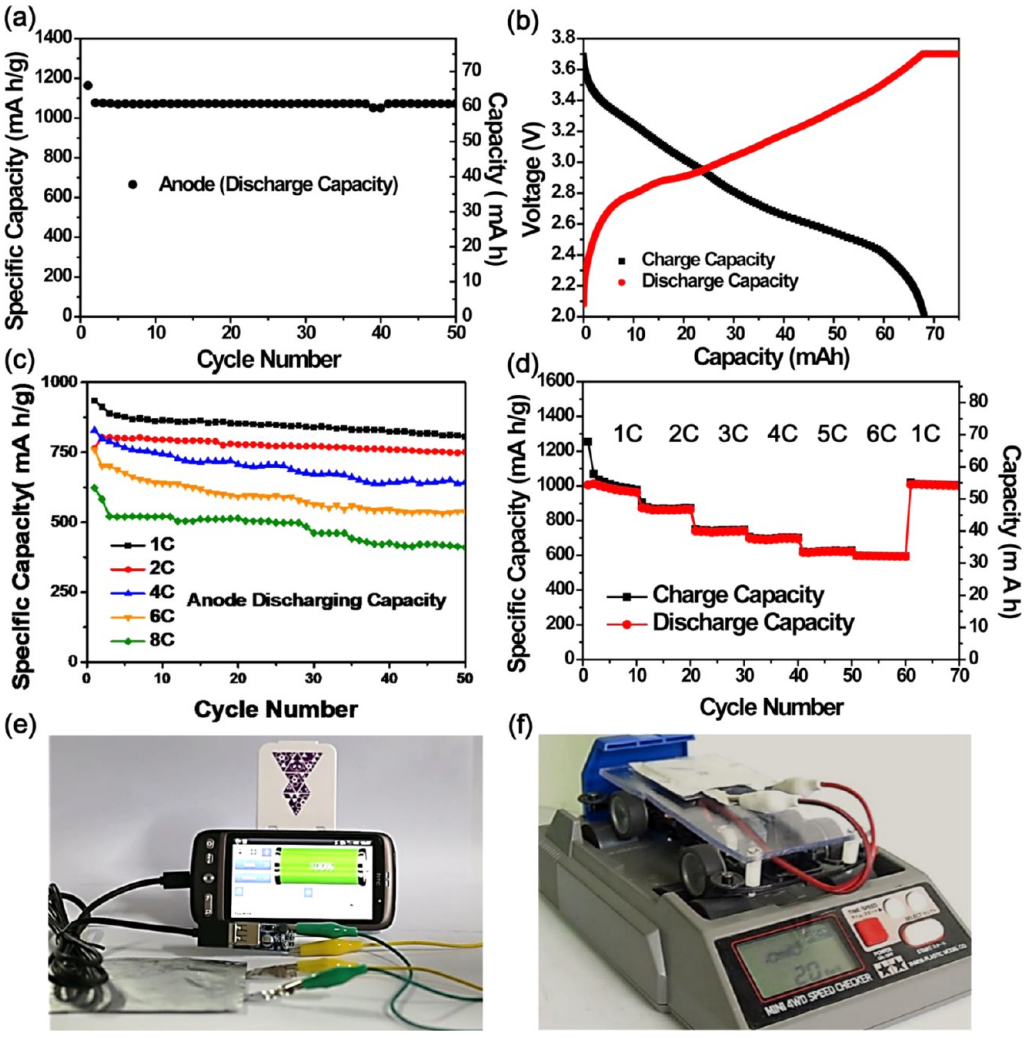

Figure 9. CuP_2 nanowire anode pouch-type full cell (cathode: $LiFePO_4$). (a) Discharge cycle performance and (b) galvanostatic charge/discharge profiles of CuP_2 nanowire at 0.1 C rate in the voltage window of 2.1 V−3.7 V in room temperature. (c) Different current densities including 1, 2, 4, 6, and 8 C for CuP_2 nanowires cycling life curve. (d) Rate capability test of CuP_2 nanowire is executed from 1, 2, 4, 6, 8 C and finally returns to 1 C. Panels e and f demonstrate a CuP_2-based pouch-type full cell application.

the Cu nanoparticles about 4−5 nm were embedded in the Li_3P matrix, in the fully charging condition, which corresponds to eq 1. While discharging to 2.5 V, a similar estimation of the *d*-spacing revealed that the phase of $LiCu_2P_2$ (0.23 nm) appeared without Li_3P and the nanowire morphology was still observed from Figure 8b. The preliminary FFT image and then the selected area electron diffraction (SAED) were applied to confirm the $LiCu_2P_2$ phase (JCPDS 72-0810) again. According to the above-mentioned conditions, we propose reasonable mechanisms such as eq 2 and eq 3:

$$2CuP_2 + 3Li^+ + 3e^- \rightarrow LiCu_2P_2 + 2LiP \quad (2)$$

$$LiCu_2P_2 + 2LiP + 9Li^+ + 9e^- \leftrightarrow 2Cu + 4Li_3P \quad (3)$$

During charging, copper phosphide reacted with Li irreversibly to transform ternary compound $LiCu_2P_2$ and LiP through a displacement reaction.[65−68] Following, more Li particles participate in the reaction producing Li_3P and copper nanoparticles associated with the conversion reaction. During a discharging process, copper and Li_3P return to $LiCu_2P_2$ and LiP instead of CuP_2. The overall reaction is the same as eq 1 in the first charge; that is to say one mole of CuP_2 can react with six moles of Li ion. On the basis of that conclusion, we calculate the theoretical capacity of CuP_2 equal to 1281 mA h g^{-1}, which nearly agrees with our electrochemical test at 0.1 C. From the above results, we speculate that CuP_2 nanowires have excellent electrochemical performance probably associated with formation of conductive metal nanoparticles and the Li_3P matrix, which enhance the conductivity of the electrode and effectively alleviate stress from volume variance during the cycle process.[69]

Full Cell Battery. We further demonstrated the lithium ion full battery for practical uses. The full cell type we fabricated was pouch cell configuration, which was composed of the CuP_2 nanowires as anode, the $LiFePO_4$/Al foil as cathode, $LiPF_6$-based electrolyte, and flexible plastic Al shell. In general, the choice of acceptable potential window and optimum areal capacity balance between anode and cathode were required for perfect full cell assembly. To decide the working potential window of a full cell, the simulated charging and discharging curves were obtained by utilizing charging/discharging curves of both the anode and cathode in a half cell. The respective potential window of anode and cathode for a half cell was adopted as largely as possible to find the complete working potential curve. The simulated charging curve of the full cell is

DOI: 10.1021/acsnano.6b03954
ACS Nano 2016, 10, 8632−8644

plotted by subtracting the discharging curve of the anode (CuP_2 nanowires) and the charging curve of the cathode ($LiFePO_4$) in their respective half cells shown in Figure S10. In a similar way, the simulated discharge curve of the full cell was obtained. On the basis of the simulated results, the potential window range from 2.1 to 3.7 V for the full cell was designed. Few capacities can be obtained below 2.1 V or above 3.7 V. Besides, the low output voltage in the full cell limits its further applications and the high voltage probably produces side reaction.

The optimum areal capacity balance is as follows:

$$\frac{A_{rev}}{C_{fc} - A_{irrev}} \approx 1$$

where A_{rev}, A_{irrev}, and C_{fc} represent the anode reversible areal capacity, anode irreversible areal capacity, and first charging areal capacity cathode, respectively. In the work, anode reversible areal capacity, the first charging areal capacity cathode, and anode irreversible areal capacity are 0.7, 1.2, and 0.6 mA h cm^{-2}, respectively. (Anode first charging areal capacity is 1.6 mA h cm^{-2} with coulombic efficiency of 63%.) Compared to the coin-type full cell, the pouch cell reduced the resistance dramatically which makes it possible to have excellent electrochemical performance. Through anode and cathode electrode capacity comparison, the total capacity of the full cell was 60 mA h, and the cycle performance was shown in Figure 9a. At the first discharge, the capacity exhibits 68 mA h at a rate of 0.1 C between 2.1 and 3.7 V, indicative of 1199 mA h g^{-1} of anode electrode. The capacities of following cycles were reduced slightly and maintained at 60.6 mA h, showing 1070 mA h g^{-1}. The slightly high capacity compared with the objective is acceptable with only 1% deviation due to optimization of the capacity ratio of the anode/cathode. Finally, the cell had a stable capacity of about 1000 mA h g^{-1}. At the same time, we carried out the high rate test for CuP_2-based full cell with capacity of 60 mA h. From Figure 9c, the specific capacity of anode material obtained at the rate of 1, 2, 4, 6, and 8 C is 850, 700, 650, 550, and 450 mA h g^{-1}, respectively, and perform acceptable capacity retention after 50 cycles. At a rate capability test, the pouch type full cell experiences 1, 2, 3, 4, 5, and 6 C and finally returns to 1 C; the specific capacity for anode material still has 950 mA g^{-1} with a retention of 97% compared to the previous 1 C test result, and the whole capacity for pouch type full cell is 54 mA h. To facilitate CuP_2 applications, a lithium ion battery was used to power different portable devices as shown in Figure 9e,f. A single battery was applied to cell phone operation and served as a mobile power bank connected to a specific chip associated with voltage control (see Movie S1 in the Supporting Information for the operation process). Meanwhile, we also trigger a model car, a Mini 4WD. Through the speedometer, the average and maximum speed of the model car powered by the full cell maintained 16 and 20 km h^{-1}, respectively (see Figure 9f and Movie S2 in the Supporting Information). The Mini 4WD loaded with the CuP_2 battery can run in a race track circuit with long track length. (see Figure S10 and Movie S3 in the Supporting Information).

CONCLUSIONS

By the SFLS method, single crystalline CuP_2 nanowires were synthesized with high yield and high aspect ratio in the presence of a Bi precursor at 410 °C pressurized to 10.2 MPa. The electrical measurement was carried out to inspect the electrical transport property of single CuP_2 nanowire, exhibiting an on/off ratio larger than 104 and a hole mobility of 147 cm^2 V^{-1} s^{-1}. CuP_2 nanowires also react with lithium by conversion reaction evidenced by *ex-situ* TEM analysis, exhibiting a distinguished capacity of 945 mA h g^{-1} after 100 cycles, aided by the 450 °C calcination treatment. The good capacity retention is due to carbon layer protection from nanomaterial aggregation and raises the conductivity of the electrode. Following, the batteries to power a model car and a mobile phone were demonstrated. Therefore, the CuP_2 nanowire becomes an appealing nanomaterial for technological improvement of the FET and energy storage due to phosphorus-rich material and an anisotropy nanostructure. Besides, the CuP_2 nanowires have the advantages of an earth-abundant supply of element and a low price of precursors. For instance, crustal abundance of copper and phosphide corresponds to 0.007 and 0.1%, respectively, representing their high earth-abundance. If the synthesis yield level increases, the CuP_2 nanowires have a chance to scale-up for commercial applications.

EXPERIMENTAL SECTION

Materials. Copper(I) chloride (99.99%) and bismuth(III) 2-ethylhexanoate were purchased from Alfa Aesar. Anhydrous benzene (99.99%), oleylamine (OLA, 70%), toluene (99.99%), ethanol (99.99%), tri-*n*-octylphosphine (TOP, 90%), and poly(acrylic acid) (PAA, average $M_v \approx 450\,000$) were purchased from Sigma-Aldrich. Celgard membrane, Li metal foil (99.9%), Cu metal foil (0.01 mm), electrolyte (1 M $LiPF_6$ in fluoro-ethylene carbonate/diethyl carbonate (FEC/DEC) (3:7 vol %)), $LiFePO_4$ cathode material, Super P carbon black, and coin cells (CR2032), were obtained from SYNergy ScienTech Corp. Al laminated film and the metallic strip terminal for pouch cell assembly were purchased from MTI Corp.

CuP_2 Nanowire Synthesis. CuP_2 nanowire was synthesized in a 10 mL titanium reactor by a SFLS growth.[70−72] The reactor was free of oxygen by placing it in an argon-filled glovebox and then brought out. The reactor was preheated to 400 °C inside a heating tank accurately controlled by a controller to prevent temperature runaway. The reactor was attached to a six-way valve equipped with a 5 mL injection loop through a high-pressure (1/8 in. i.d.) tubing. The stock solution was delivered into the pressurized reactor by a high pressure liquid chromatography (HPLC) pump (Lab Alliance, series 1500). Furthermore, 1 mmol copper chloride powder was dissolved in 6 mL of TOP in which the metal−TOP complex quickly formed while heating up the solution to 150 °C in a glovebox. Meanwhile, bismuth 2-ethylhexanoate in OLA with concentration 0.02 M was prepared as seeds for nanowire growth. The reactant to bismuth precursor mole ratio used in the reaction was 3000:1. While the reactor was heated to 410 °C and pressurized to 5.4 MPa, the 5 mL precursor solution was injected into the injection loop and delivered to the reactor at a flow rate of 0.5 mL min^{-1}. After the pressure reached 13.6 MPa, the reactor cell was cooled by a water bath back to room temperature, and finally CuP_2 nanowires were taken out from the reactor for further uses.

Characterization. CuP_2 nanowires were characterized by SEM, TEM, EDS, XPS, and XRD. To obtain HRSEM images of CuP_2 nanowires, a HITACHI-S4800 field-emission SEM with 10 kV accelerating voltage and 8 mm working distance was utilized. The TEM samples were prepared by drop-casting nanowires dispersed in toluene onto 200 mesh lacey carbon-coated copper grids and dried in vacuum oven overnight. Meanwhile, EDS was carried out for element confirmation with as-prepared samples on nickel grids. XRD patterns were gained by a Shimadzu XRD-6000 diffractometer equipped with Cu Kα radiation. High resolution XPS measurements were taken on a PHI Quantera SXM to examine surface states of CuP_2 nanowires. While carrying out *ex-situ* TEM analysis of the samples after electrochemical reaction, the electrode material was detached from

DOI: 10.1021/acsnano.6b03954
ACS Nano 2016, 10, 8632−8644

the current collector and dispersed in DEC with ultrasonic treatment to remove organic residues and lithium salts.

To study the transistor properties, CuP_2 nanowires were spread onto a SiO_2/Si substrate that was about 300 nm thick for top thermal SiO_2. The heavily doped Si substrate possesses a resistivity of 1−5 mΩ cm and serves as a back-gate for device characterization. Then Ni contacts were defined to CuP_2 nanowires using e-beam lithography (EBL). The sample was immersed into diluted hydrofluoric acid for seconds to completely eliminating native oxide in the contact region before e-beam evaporation of Ni.

Lithium-Ion Battery Assembly and Electrochemical Characterization. The homogeneous slurry for anode electrode was prepared by mixing active materials (CuP_2 nanowire, 70 wt %) with 15 wt % of Super-P and 15 wt % of PAA binder dispersed in ethanol solvent. Then the slurry prepared was spread onto a copper foil by an automatic thick film coating machine to ensure the uniformity of the electrode thickness. The electrode was dried at 50 °C in a vacuum oven to evaporate the solvent and then 120 °C under argon gas for removing residual water. After being densely pressed by a rolling press machine, the electrode was cut into a circle shape with a diameter of 12 mm for the coin cell. Utilizing a microbalance with 0.1 μg resolution (Sartorius SE2), accurate weight of the pure active material was measured for calculating the material capacity. Typical mass loading on the anode electrode was ∼1 mg cm^{-2} total and 0.7 mg cm^{-2} active. Before assembling the batteries, the removal of water and oxygen in the anode electrode was executed in the dryer for 24 h. The CuP_2-based anode, Li-metal cathode, and electrolyte-wetted celgard membrane were stacked evenly for CR2032 coin cell assembly in the glovebox. Electrochemical performance of the CuP_2 nanowires was assessed by employing Maccor Series 4000 instruments. For a pouch-type fuel cell assembly, the cathode Li metal was replaced by $LiFePO_4$. The mass loading ratio of CuP_2 nanowires to $LiFePO_4$ in the fuel cell is 0.7 mg cm^{-2} to 6.88 mg cm^{-2} (anode areal capacity of 0.7 mA h cm^{-2} and cathode areal capacity of 1.1 mA h cm^{-2}). Anode and cathode electrodes were cut into 60 cm^2 area and separated by a polyethylene membrane, fixed tightly by tape before welding the metallic strip terminal. The cell was sealed inside the cup-shaped Al laminated film, leaving one side open. The partly finished product was taken into the glovebox for electrolyte filling and sealing. Before inspection of the electrochemical properties, the pouch cell and coin cell were allowed to rest for half an hour to ensure complete electrolyte soaking. The cell was then examined at a current density of 0.1 C (1 C = 1A g^{-1}) in voltage windows between 2.1 and 3.7 V by a battery analyzer.

ASSOCIATED CONTENT

Supporting Information

The Supporting Information is available free of charge on the ACS Publications website at DOI: 10.1021/acsnano.6b03954.

TEM images of CuP_2 nanowires synthesized with different precursor; XPS of CuP_2 nanowire exposure to atmosphere after a month; XRD, SEM, and TEM images of calcined CuP_2 nanowires; SEM images of CuP_2 nanowires before/after cycling tests; electrode after cycling tests; cycling life curve of CuP_2 wires for 200 cycles at 1 C and SEM images for electrode morphology change before/after reaction; CV test of CuP_2 nanowire without calcination; comparison of calcined/without calcined CuP_2 nanowires at EIS test; simulation of charging/discgarging curve of fuel cell (PDF)

Single battery serving as a mobile power bank (MPG)

Model car powered by a fuel cell (MPG)

Model car, powered by a fuel cell, running on a track (MPG)

AUTHOR INFORMATION

Corresponding Author

*E-mail: hytuan@che.nthu.edu.

Notes

The authors declare no competing financial interest.

ACKNOWLEDGMENTS

We acknowledge the financial support by the Ministry of Science and Technology through the grants of NSC 102-2221-E-007-023-MY3, MOST 103-2221-E-007-089-MY3, MOST 103-2622-E-007-025, and MOST 102−2633-M-007-002.

REFERENCES

(1) Chen, J. H.; Tai, M. F.; Chi, K. M. Catalytic Synthesis, Characterization and Magnetic Properties of Iron Phosphide Nanowires. *J. Mater. Chem.* **2004**, *14*, 296−298.

(2) Qian, C.; Kim, F.; Ma, L.; Tsui, F.; Yang, P. D.; Liu, J. Solution-Phase Synthesis of Single-Crystalline Iron Phosphide Nanorods/Nanowires. *J. Am. Chem. Soc.* **2004**, *126*, 1195−1198.

(3) Yang, R. S.; Chueh, Y. L.; Morber, J. R.; Snyder, R.; Chou, L. J.; Wang, Z. L. Single-Crystalline Branched Zinc Phosphide Nanostructures: Synthesis, Properties, and Optoelectronic Devices. *Nano Lett.* **2007**, *7*, 269−275.

(4) Kornienko, N.; Whitmore, D. D.; Yu, Y.; Leone, S. R.; Yang, P. D. Solution Phase Synthesis of Indium Gallium Phosphide Alloy Nanowires. *ACS Nano* **2015**, *9*, 3951−3960.

(5) Assali, S.; Zardo, I.; Plissard, S.; Kriegner, D.; Verheijen, M. A.; Bauer, G.; Meijerink, A.; Belabbes, A.; Bechstedt, F.; Haverkort, J. E. M.; Bakkers, E. P. A. M. Direct Band Gap Wurtzite Gallium Phosphide Nanowires. *Nano Lett.* **2013**, *13*, 1559−1563.

(6) Luber, E. J.; Mobarok, M. H.; Buriak, J. M. Solution-Processed Zinc Phosphide (Alpha-Zn_3P_2) Colloidal Semiconducting Nanocrystals for Thin Film Photovoltaic Applications. *ACS Nano* **2013**, *7*, 8136−8146.

(7) Duan, X. F.; Huang, Y.; Cui, Y.; Wang, J. F.; Lieber, C. M. Indium Phosphide Nanowires as Building Blocks for Nanoscale Electronic and Optoelectronic Devices. *Nature* **2001**, *409*, 66−69.

(8) Souza, D. C. S.; Pralong, V.; Jacobson, A. J.; Nazar, L. F. A Reversible Solid-State Crystalline Transformation in a Metal Phosphide Induced by Redox Chemistry. *Science* **2002**, *296*, 2012−2015.

(9) Kim, Y.; Kim, Y.; Choi, A.; Woo, S.; Mok, D.; Choi, N. S.; Jung, Y. S.; Ryu, J. H.; Oh, S. M.; Lee, K. T. Tin Phosphide as a Promising Anode Material for Na-Ion Batteries. *Adv. Mater.* **2014**, *26*, 4139−4144.

(10) Stan, M. C.; Klopsch, R.; Bhaskar, A.; Li, J.; Passerini, S.; Winter, M. Cu_3P Binary Phosphide: Synthesis *via* a Wet Mechanochemical Method and Electrochemical Behavior as Negative Electrode Material for Lithium-Ion Batteries. *Adv. Energy Mater.* **2013**, *3*, 231−238.

(11) Lu, Y.; Tu, J. P.; Xiong, Q. Q.; Xiang, J. Y.; Mai, Y. J.; Zhang, J.; Qiao, Y. Q.; Wang, X. L.; Gu, C. D.; Mao, S. X. Controllable Synthesis of a Monophase Nickel Phosphide/Carbon (Ni_5P_4/C) Composite Electrode *via* Wet-Chemistry and a Solid-State Reaction for the Anode in Lithium Secondary Batteries. *Adv. Funct. Mater.* **2012**, *22*, 3927−3935.

(12) Hall, J. W.; Membreno, N.; Wu, J.; Celio, H.; Jones, R. A.; Stevenson, K. J. Low-Temperature Synthesis of Amorphous FeP_2 and Its Use as Anodes for Li Ion Batteries. *J. Am. Chem. Soc.* **2012**, *134*, 5532−5535.

(13) Zhang, H. J.; Feng, Y. Y.; Zhang, Y.; Fang, L.; Li, W. X.; Liu, Q.; Wu, K.; Wang, Y. Peapod-Like Composite with Nickel Phosphide Nanoparticles Encapsulated in Carbon Fibers as Enhanced Anode for Li-Ion Batteries. *ChemSusChem* **2014**, *7*, 2000−2006.

(14) Zhou, K.; Zhou, W. J.; Yang, L. J.; Lu, J.; Cheng, S.; Mai, W. J.; Tang, Z. H.; Li, L. G.; Chen, S. W. Ultrahigh-Performance Pseudocapacitor Electrodes Based on Transition Metal Phosphide

DOI: 10.1021/acsnano.6b03954
ACS Nano 2016, 10, 8632−8644

Nanosheets Array *via* Phosphorization: A General and Effective Approach. *Adv. Funct. Mater.* **2015**, *25*, 7530−7538.
(15) Wang, J. L.; Yang, Q.; Zhang, Z. D.; Sun, S. H. Phase-Controlled Synthesis of Transition-Metal Phosphide Nanowires by Ullmann-Type Reactions. *Chem. - Eur. J.* **2010**, *16*, 7916−7924.
(16) Muthuswamy, E.; Savithra, G. H. L.; Brock, S. L. Synthetic Levers Enabling Independent Control of Phase, Size, and Morphology in Nickel Phosphide Nanoparticles. *ACS Nano* **2011**, *5*, 2402−2411.
(17) Muthuswamy, E.; Kharel, P. R.; Lawes, G.; Brock, S. L. Control of Phase in Phosphide Nanoparticles Produced by Metal Nanoparticle Transformation: Fe_2P and FeP. *ACS Nano* **2009**, *3*, 2383−2393.
(18) Wu, J.; Chong, X. Y.; Zhou, R.; Jiang, Y. H.; Feng, J. Structure, Stability, Mechanical and Electronic Properties of Fe-P Binary Compounds by First-Principles Calculations. *RSC Adv.* **2015**, *5*, 81943−81956.
(19) Arico, A. S.; Bruce, P.; Scrosati, B.; Tarascon, J. M.; Van Schalkwijk, W. Nanostructured Materials for Advanced Energy Conversion and Storage Devices. *Nat. Mater.* **2005**, *4*, 366−377.
(20) Carenco, S.; Portehault, D.; Boissiere, C.; Mezailles, N.; Sanchez, C. Nanoscaled Metal Borides and Phosphides: Recent Developments and Perspectives. *Chem. Rev.* **2013**, *113*, 7981−8065.
(21) Carenco, S.; Portehault, D.; Boissiere, C.; Mezailles, N.; Sanchez, C. 25th Anniversary Article: Exploring Nanoscaled Matter from Speciation to Phase Diagrams: Metal Phosphide Nanoparticles as a Case of Study. *Adv. Mater.* **2014**, *26*, 371−389.
(22) Brock, S. L.; Perera, S. C.; Stamm, K. L. Chemical Routes for Production of Transition-Metal Phosphides on the Nanoscale: Implications for Advanced Magnetic and Catalytic Materials. *Chem. - Eur. J.* **2004**, *10*, 3364−3371.
(23) McVey, B. F. P.; Butkus, J.; Halpert, J. E.; Hodgkiss, J. M.; Tilley, R. D. Solution Synthesis and Optical Properties of Transition-Metal-Doped Silicon Nanocrystals. *J. Phys. Chem. Lett.* **2015**, *6*, 1573−1576.
(24) Cui, Y.; Zhong, Z. H.; Wang, D. L.; Wang, W. U.; Lieber, C. M. High Performance Silicon Nanowire Field Effect Transistors. *Nano Lett.* **2003**, *3*, 149−152.
(25) Ford, A. C.; Ho, J. C.; Chueh, Y. L.; Tseng, Y. C.; Fan, Z. Y.; Guo, J.; Bokor, J.; Javey, A. Diameter-Dependent Electron Mobility of Inas Nanowires. *Nano Lett.* **2009**, *9*, 360−365.
(26) Friedman, R. S.; McAlpine, M. C.; Ricketts, D. S.; Ham, D.; Lieber, C. M. High-Speed Integrated Nanowire Circuits. *Nature* **2005**, *434*, 1085−1085.
(27) Duan, X. F.; Niu, C. M.; Sahi, V.; Chen, J.; Parce, J. W.; Empedocles, S.; Goldman, J. L. High-Performance Thin-Film Transistors Using Semiconductor Nanowires and Nanoribbons. *Nature* **2003**, *425*, 274−278.
(28) Park, C. M.; Sohn, H. J. Black Phosphorus and Its Composite for Lithium Rechargeable Batteries. *Adv. Mater.* **2007**, *19*, 2465−2468.
(29) Wang, L.; He, X. M.; Li, J. J.; Sun, W. T.; Gao, J.; Guo, J. W.; Jiang, C. Y. Nano-Structured Phosphorus Composite as High-Capacity Anode Materials for Lithium Batteries. *Angew. Chem., Int. Ed.* **2012**, *51*, 9034−9037.
(30) Sun, J.; Zheng, G. Y.; Lee, H. W.; Liu, N.; Wang, H. T.; Yao, H. B.; Yang, W. S.; Cui, Y. Formation of Stable Phosphorus-Carbon Bond for Enhanced Performance in Black Phosphorus Nanoparticle-Graphite Composite Battery Anodes. *Nano Lett.* **2014**, *14*, 4573−4580.
(31) Qian, J. F.; Qiao, D.; Ai, X. P.; Cao, Y. L.; Yang, H. X. Reversible 3-Li Storage Reactions of Amorphous Phosphorus as High Capacity and Cycling-Stable Anodes for Li-Ion Batteries. *Chem. Commun.* **2012**, *48*, 8931−8933.
(32) Kloc, C.; Luxsteiner, M. C.; Keil, M.; Baumann, J. R.; Doll, G.; Bucher, E. Growth and Characterization of CuP_2 Single-Crystals. *J. Cryst. Growth* **1990**, *106*, 635−642.
(33) Odile, J. P.; Soled, S.; Castro, C. A.; Wold, A. Crystal-Growth and Characterization of Transition-Metal Phosphides CuP_2, NiP_2, and RhP_3. *Inorg. Chem.* **1978**, *17*, 283−286.
(34) Muller, M. H.; Jeitschko, W. Preparation, Properties, and Crystal-Structure of Cu_2P_7 and Structure Refinements of CuP_2 and AgP_2. *Z. Anorg. Allg. Chem.* **1982**, *491*, 225−236.
(35) Wang, K.; Yang, J.; Xie, J. Y.; Wang, B. F.; Wen, Z. S. Electrochemical Reactions of Lithium with CuP_2 and $Li_{1.75}Cu_{1.25}P_2$ Synthesized by Ballmilling. *Electrochem. Commun.* **2003**, *5*, 480−483.
(36) McGrath, A. J.; Chien, Y.-H.; Cheong, S.; Herman, D. A. J.; Watt, J.; Henning, A. M.; Gloag, L.; Yeh, C.-S.; Tilley, R. D. Gold over Branched Palladium Nanostructures for Photothermal Cancer Therapy. *ACS Nano* **2015**, *9*, 12283−12291.
(37) Olofsson, O. Crystal Structures of CuP_2 and AgP_2 with Some Phase Analytical Data of Cu-P and Ag-P Systems. *Acta Chem. Scand.* **1965**, *19*, 229−241.
(38) Zhang, S. Y.; Ye, E. Y.; Liu, S. H.; Lim, S. H.; Tee, S. Y.; Dong, Z. L.; Han, M. Y. Temperature and Chemical Bonding-Directed Self-Assembly of Cobalt Phosphide Nanowires in Reaction Solutions into Vertical and Horizontal Alignments. *Adv. Mater.* **2012**, *24*, 4369−4375.
(39) Davidson, F. M.; Wiacek, R.; Korgel, B. A. Supercritical Fluid-Liquid-Solid Synthesis of Gallium Phosphide Nanowires. *Chem. Mater.* **2005**, *17*, 230−233.
(40) Davidson, F. M.; Schricker, A. D.; Wiacek, R. J.; Korgel, B. A. Supercritical Fluid-Liquid-Solid Synthesis of Gallium Arsenide Nanowires Seeded by Alkanethiol-Stabilized Gold Nanocrystals. *Adv. Mater.* **2004**, *16*, 646−649.
(41) Lee, D. C.; Hanrath, T.; Korgel, B. A. The Role of Precursor-Decomposition Kinetics in Silicon-Nanowire Synthesis in Organic Solvents. *Angew. Chem., Int. Ed.* **2005**, *44*, 3573−3577.
(42) Yang, H. J.; Tuan, H. Y. High-Yield, High-Throughput Synthesis of Germanium Nanowires by Metal-Organic Chemical Vapor Deposition and Their Functionalization and Applications. *J. Mater. Chem.* **2012**, *22*, 2215−2225.
(43) Bawohl, M.; Nilges, T. Phosphorus Rich D(10) Ion Polyphosphides and Selected Materials. *Z. Anorg. Allg. Chem.* **2015**, *641*, 304−310.
(44) Kim, C. J.; Lee, H. S.; Cho, Y. J.; Kang, K.; Jo, M. H. Diameter-Dependent Internal Gain in Ohmic Ge Nanowire Photodetectors. *Nano Lett.* **2010**, *10*, 2043−2048.
(45) Wunnicke, O. Gate Capacitance of Back-Gated Nanowire Field-Effect Transistors. *Appl. Phys. Lett.* **2006**, *89*, 083102.
(46) Tang, J. S.; Wang, C. Y.; Xiu, F. X.; Hong, A. J.; Chen, S. Y.; Wang, M. S.; Zeng, C. F.; Yang, H. J.; Tuan, H. Y.; Tsai, C. J.; Chen, L. J.; Wang, K. L. Single-Crystalline Ni_2Ge/Ge/Ni_2Ge Nanowire Heterostructure Transistors. *Nanotechnology* **2010**, *21*, 505704.
(47) Tang, J. S.; Wang, C. Y.; Xiu, F. X.; Lang, M. R.; Chu, L. W.; Tsai, C. J.; Chueh, Y. L.; Chen, L. J.; Wang, K. L. Oxide-Confined Formation of Germanium Nanowire Heterostructures for High-Performance Transistors. *ACS Nano* **2011**, *5*, 6008−6015.
(48) Tang, J. S.; Wang, C. Y.; Hung, M. H.; Jiang, X. W.; Chang, L. T.; He, L.; Liu, P. H.; Yang, H. J.; Tuan, H. Y.; Chen, L. J.; Wang, K. L. Ferromagnetic Germanide in Ge Nanowire Transistors for Spintronics Application. *ACS Nano* **2012**, *6*, 5710−5717.
(49) Wu, H.; Chan, G.; Choi, J. W.; Ryu, I.; Yao, Y.; McDowell, M. T.; Lee, S. W.; Jackson, A.; Yang, Y.; Hu, L. B.; Cui, Y. Stable Cycling of Double-Walled Silicon Nanotube Battery Anodes through Solid-Electrolyte Interphase Control. *Nat. Nanotechnol.* **2012**, *7*, 309−314.
(50) Wu, H.; Yu, G. H.; Pan, L. J.; Liu, N. A.; McDowell, M. T.; Bao, Z. A.; Cui, Y. Stable Li-Ion Battery Anodes by *in-Situ* Polymerization of Conducting Hydrogel to Conformally Coat Silicon Nanoparticles. *Nat. Commun.* **2013**, *4*, 1943.
(51) Liu, N.; Lu, Z. D.; Zhao, J.; McDowell, M. T.; Lee, H. W.; Zhao, W. T.; Cui, Y. A Pomegranate-Inspired Nanoscale Design for Large-Volume-Change Lithium Battery Anodes. *Nat. Nanotechnol.* **2014**, *9*, 187−192.
(52) Hwang, J.; Jo, C.; Kim, M. G.; Chun, J.; Lim, E.; Kim, S.; Jeong, S.; Kim, Y.; Lee, J. Mesoporous Ge/GeO_2/Carbon Lithium-Ion Battery Anodes with High Capacity and High Reversibility. *ACS Nano* **2015**, *9*, 5299−5309.
(53) Carenco, S.; Surcin, C.; Morcrette, M.; Larcher, D.; Mezailles, N.; Boissiere, C.; Sanchez, C. Improving the Li-Electrochemical

DOI: 10.1021/acsnano.6b03954
ACS Nano 2016, 10, 8632−8644

Properties of Monodisperse Ni_2P Nanoparticles by Self-Generated Carbon Coating. *Chem. Mater.* **2012**, *24*, 688−697.
(54) Lee, K. T.; Jung, Y. S.; Oh, S. M. Synthesis of Tin-Encapsulated Spherical Hollow Carbon for Anode Material in Lithium Secondary Batteries. *J. Am. Chem. Soc.* **2003**, *125*, 5652−5653.
(55) Fu, L. J.; Liu, H.; Zhang, H. P.; Li, C.; Zhang, T.; Wu, Y. P.; Holze, R.; Wu, H. Q. Synthesis and Electrochemical Performance of Novel Core/Shell Structured Nanocomposites. *Electrochem. Commun.* **2006**, *8*, 1−4.
(56) Kennedy, T.; Bezuidenhout, M.; Palaniappan, K.; Stokes, K.; Brandon, M.; Ryan, K. M. Nanowire Heterostructures Comprising Germanium Stems and Silicon Branches as High-Capacity Li-Ion Anodes with Tunable Rate Capability. *ACS Nano* **2015**, *9*, 7456−7465.
(57) Wang, F.; Robert, R.; Chernova, N. A.; Pereira, N.; Omenya, F.; Badway, F.; Hua, X.; Ruotolo, M.; Zhang, R. G.; Wu, L. J.; Volkov, V.; Su, D.; Key, B.; Whittingham, M. S.; Grey, C. P.; Amatucci, G. G.; Zhu, Y. M.; Graetz, J. Conversion Reaction Mechanisms in Lithium Ion Batteries: Study of the Binary Metal Fluoride Electrodes. *J. Am. Chem. Soc.* **2011**, *133*, 18828−18836.
(58) Boyanov, S.; Bernardi, J.; Gillot, F.; Dupont, L.; Womes, M.; Tarascon, J. M.; Monconduit, L.; Doublet, M. L. Fep: Another Attractive Anode for the Li-Ion Battery Enlisting a Reversible Two-Step Insertion/Conversion Process. *Chem. Mater.* **2006**, *18*, 3531−3538.
(59) Shi, Y.; Wen, L.; Li, F.; Cheng, H. M. Nanosized $Li_4Ti_5O_{12}$/Graphene Hybrid Materials with Low Polarization for High Rate Lithium Ion Batteries. *J. Power Sources* **2011**, *196*, 8610−8617.
(60) Taberna, L.; Mitra, S.; Poizot, P.; Simon, P.; Tarascon, J. M. High Rate Capabilities Fe_3O_4-Based Cu Nano-Architectured Electrodes for Lithium-Ion Battery Applications. *Nat. Mater.* **2006**, *5*, 567−573.
(61) Jossen, A. Fundamentals of Battery Dynamics. *J. Power Sources* **2006**, *154*, 530−538.
(62) Sun, Y. M.; Hu, X. L.; Luo, W.; Xia, F. F.; Huang, Y. H. Reconstruction of Conformal Nanoscale Mno on Graphene as a High-Capacity and Long-Life Anode Material for Lithium Ion Batteries. *Adv. Funct. Mater.* **2013**, *23*, 2436−2444.
(63) Ueda, A.; Nagao, M.; Inoue, A.; Hayashi, A.; Seino, Y.; Ota, T.; Tatsumisago, M. Electrochemical Performance of All-Solid-State Lithium Batteries with Sn_4P_3 Negative Electrode. *J. Power Sources* **2013**, *244*, 597−600.
(64) Kwon, H.-T.; Lee, C. K.; Jeon, K.-J.; Park, C.-M. Silicon Diphosphide: A Si-Based Three-Dimensional Crystalline Framework as a High-Performance Li-Ion Battery Anode. *ACS Nano* **2016**, *10*, 5701−5709.
(65) Klein, F.; Jache, B.; Bhide, A.; Adelhelm, P. Conversion Reactions for Sodium-Ion Batteries. *Phys. Chem. Chem. Phys.* **2013**, *15*, 15876−15887.
(66) Crosnier, O.; Nazar, L. F. Facile Reversible Displacement Reaction of Cu_3P with Lithium at Low Potential. *Electrochem. Solid-State Lett.* **2004**, *7*, A187−A189.
(67) Pralong, V.; Souza, D. C. S.; Leung, K. T.; Nazar, L. F. Reversible Lithium Uptake by CoP_3 at Low Potential: Role of the Anion. *Electrochem. Commun.* **2002**, *4*, 516−520.
(68) Zhang, W. Q.; Yang, J. Z.; Lu, X. M. Tailoring Galvanic Replacement Reaction for the Preparation of Pt/Ag Bimetallic Hollow Nanostructures with Controlled Number of Voids. *ACS Nano* **2012**, *6*, 7397−7405.
(69) Kennedy, T.; Mullane, E.; Geaney, H.; Osiak, M.; O'Dwyer, C.; Ryan, K. M. High-Performance Germanium Nanowire-Based Lithium-Ion Battery Anodes Extending over 1000 Cycles through *in Situ* Formation of a Continuous Porous Network. *Nano Lett.* **2014**, *14*, 716−723.
(70) Davidson, F. M.; Wiacek, R.; Korgel, B. A. Supercritical Fluid−Liquid−Solid Synthesis of Gallium Phosphide Nanowires. *Chem. Mater.* **2005**, *17*, 230−233.
(71) Heitsch, A. T.; Akhavan, V. A.; Korgel, B. A. Rapid Sfls Synthesis of Si Nanowires Using Trisilane with *in Situ* Alkyl-Amine Passivation. *Chem. Mater.* **2011**, *23*, 2697−2699.
(72) Hanrath, T.; Korgel, B. A. Supercritical Fluid−Liquid−Solid (SFLS) Synthesis of Si and Ge Nanowires Seeded by Colloidal Metal Nanocrystals. *Adv. Mater.* **2003**, *15*, 437−440.

DOI: 10.1021/acsnano.6b03954
ACS Nano 2016, 10, 8632−8644